# Ocean gravity waves generated by the meteotsunami at the Japan Trench following the 2022 Tonga volcanic eruption

Ho, Tung-Cheng; Mori, Nobuhito; Yamada, Masumi

Ho, Tung-Cheng ...[et al]. Ocean gravity waves generated by the meteotsunami at the Japan Trench following the 2022 Tonga volcanic eruption. Earth, Planets and Space 2023, 75: 25.

Ho *et al. Earth, Planets and Space* (2023) 75:25
https://doi.org/10.1186/s40623-023-01775-x

Earth, Planets and Space

EXPRESS LETTER

Open Access

# Ocean gravity waves generated by the meteotsunami at the Japan Trench following the 2022 Tonga volcanic eruption

Tung-Cheng Ho*, Nobuhito Mori and Masumi Yamada

**Abstract**

The 2022 eruption of the Hunga Tonga-Hunga Ha'apai volcano excited an atmospheric Lamb wave, which induced a fast-traveling tsunami. This tsunami was driven by the pressure-forced wave traveling at the speed of the Lamb wave and, thus, was much faster than conventional tsunamis. This was the first case in which ocean bottom monitoring systems widely observed an air pressure-induced tsunami. We found that the pressure-forced waves split and generated ocean gravity waves after passing the Japan Trench based on the S-net data. Our simulations show that changes in water depth can amplify or decrease the pressure-forced wave. Simultaneously, an ocean gravity wave is generated due to the conservation of water volume. Because the ocean gravity wave was slower than the pressure-forced wave near Japan, it was separated from, and traveled behind, the pressure-forced wave. We explained the wave separation phenomenon and reproduced the waveforms of different splitting stages observed by the stations near the Japan Trench.

**Keywords** Tonga, Tsunami, S-net, Pressure wave, Meteotsunami, Wave split, Wave separation, Volcano, Wave deformation, Gravity wave

---

*Correspondence:
Tung-Cheng Ho
tungcheng@18.alumni.u-tokyo.ac.jp
Full list of author information is available at the end of the article

## Graphical Abstract

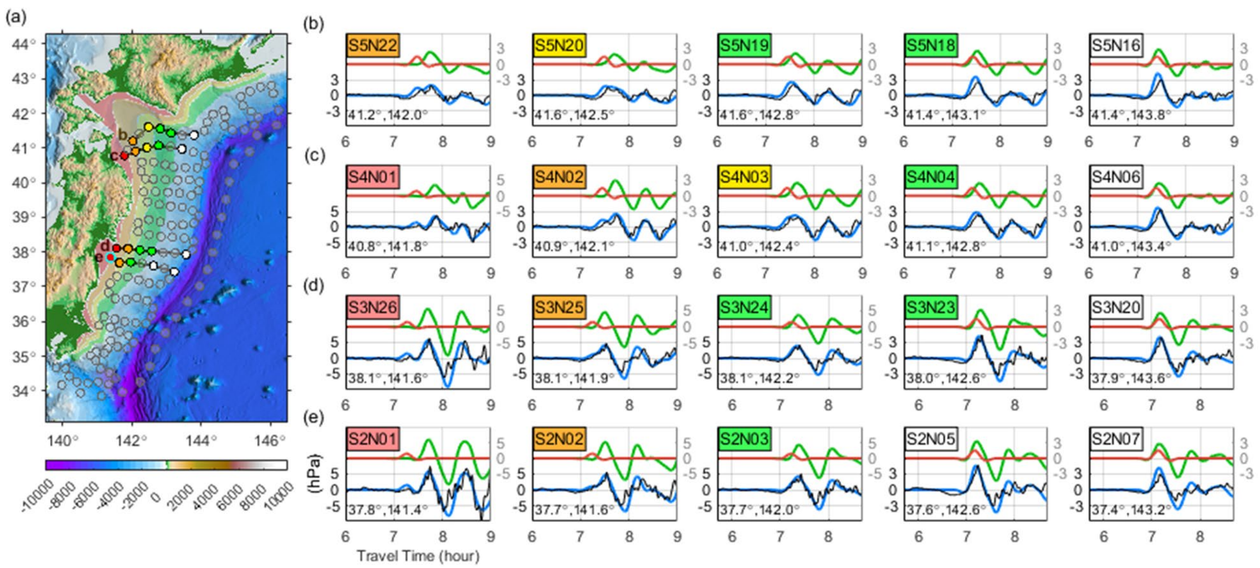

## Introduction

The Hunga Tonga-Hunga Ha'apai volcano, located in the Kingdom of Tonga in the South Pacific, approximately 65 km north of the Tongan capital island of Tongatapu, erupted violently at UTC 04:14, 15 January 2022 (USGS). After the eruption, global tsunami monitoring systems and tide gauges observed tsunami signals earlier than theoretically expected for tsunami waves (Carvajal et al. 2022). Furthermore, the recorded data revealed that the tsunami traveled at a speed of approximately 300–315 m/s (Kubota et al. 2022; Yamada et al. 2022), much faster than the conventional tsunami speed of approximately 200 m/s for an average ocean depth of 4 km.

The fast-traveling tsunami wave, which was a type of meteotsunami (Hibiya and Kajiura 1982; Monserrat et al. 2006; Rabinovich 2020; Vilibić et al. 2016), was caused by the air pressure pulse excited by the eruption, a pulse known as a Lamb wave (Lamb 1911; Matoza et al. 2022). At the source, the Lamb wave induced a sea surface disturbance (hereafter referred to as a pressure-forced wave), and ocean gravity waves were simultaneously generated due to the conservation of mass (Kubota et al. 2022). The pressure-forced wave traveled at the speed of the Lamb wave, which is much faster than the ocean gravity waves, which traveled at the long wave speed, $\sqrt{gh}$, where $g$ is gravity acceleration and $h$ is the water depth. As a result, pressure-forced waves were observed in Japan a few hours earlier than would otherwise be predicted from conventional tsunami speeds and are called fast-traveling tsunamis (Kubota et al. 2022).

Following the eruption of the Krakatau volcano in 1883, it was proposed that pressure-forced waves could generate ocean gravity waves when traversing major water depth changes (Garrett 1970). The eruption in Tonga was the first event in which ocean bottom pressure gauges (OBPGs) widely observed pressure-forced waves. In addition, the densely distributed tsunami monitoring system near the Japan Trench, S-net, observed the wave "splitting" that one pressure-forced wave split into two waves after passing the trench. Tanioka et al. (2022) reported separate waves observed by OBPGs near the Japan Trench. They performed a one-dimensional air–sea coupling simulation with a simple bathymetry synthetic test and indicated that the separation effect is sensitive to the wavelength of the Lamb wave. Yamada et al. (2022) noted that the arrival times of the disturbances at the OBPGs were almost the same as the arrival of the Lamb wave. However, those sea surface disturbances observed at tide gauges were further delayed because the separated tsunami, when passing the continental slope, traveled at the speed of the ocean gravity wave.

To understand the mechanism of complex tsunami wave splitting, we performed two-dimensional simulations of synthetic tests and considered a case study with actual bathymetry. We first discuss the relationship between the water depth and the amplitude change of the pressure-forced wave that was associated with the generation of the ocean gravity wave. We then apply our method to reproduce the observations following the Tonga eruption. It is suggested that tsunami wave splitting is associated with the amplitude change of the pressure-forced wave due to changes in water depth.

## Data and methods

### Observation data

We used air pressure data and ocean bottom pressure (OBP) data in our analyses. The air pressure data were recorded by barometers from the Incorporated Research Institutions for Seismology (IRIS) and the Japan Coast Guard (JCG). The OBP data recorded the ocean bottom pressure changes due to the air pressure pulses and sea surface waves. We utilized OBP data from S-net (Seafloor Observation Network for Earthquakes and Tsunamis along the Japan Trench) and DONET (Dense Oceanfloor Network for Earthquakes and Tsunamis). The S-net comprises 150 stations distributed off northeast Japan (Tohoku) near the Japan Trench. The DONET consists of approximately 50 stations located off south Japan near the Nankai Trough. We processed all data via the non-causal 3rd order Butterworth filter, where a bandpass filter with corner frequencies of 1/300 and 1/6000 Hz was applied to remove unrelated signals.

### Tsunami computation

We performed air–sea coupling simulations using two-dimensional linear shallow water equations in Cartesian coordinates (Woodruff et al. 2018). The continuity equation is given by

$$\frac{\partial \eta}{\partial t}+\frac{\partial (hu)}{\partial x}+\frac{\partial (hv)}{\partial y}=0, \tag{1}$$

where $u$ and $v$ are the velocities along the $x$ and $y$ directions, $h$ is still water depth, and $\eta$ is sea surface vertical displacement or sea-surface height change. We incorporated the effects of air pressure variation into the momentum equations following the long-wave approximation. The pressure combined with the hydrostatic pressure and air pressure variation is given by $P=\rho g\eta+P_{\mathrm{air}}$, where $g$ and $\rho$ are the gravitational acceleration and water density. $P_{\mathrm{air}}$ is the air pressure variation that triggers meteorological tsunami waves [refer to Saito et al. (2021) for details]. The momentum equations with air pressures are then given by (Gill 1982; Saito et al. 2021; Kubota et al. 2022):

$$\frac{\partial u}{\partial t}=-\frac{1}{\rho}\frac{\partial P_{\mathrm{air}}}{\partial x}-g\frac{\partial \eta}{\partial x}, \tag{2}$$

$$\frac{\partial v}{\partial t}=-\frac{1}{\rho}\frac{\partial P_{\mathrm{air}}}{\partial y}-g\frac{\partial \eta}{\partial y}. \tag{3}$$

The assumption of $P_{\mathrm{air}}$ for modeling the observed Lamb wave is introduced in the following section.

For the OBPGs, the ocean bottom pressure variation is given by $P_{\mathrm{OBP}}=P_{\mathrm{water}}+P_{\mathrm{air}}$, where $P_{\mathrm{water}}=\rho g\eta$ (Saito et al. 2021; Kubota et al. 2022). The ocean water density at the sea surface ranges approximately 1025–1030 kg/m$^3$, so the static water pressure at a sea surface height of 1 cm is approximately 1.01 hPa. Thus, to incorporate the OBP data with sea surface height, we approximated $P_{\mathrm{water}}=1$ hPa when sea surface height equals 1 cm in our analyses (Vennell 2010).

We applied the model of a hybrid finite volume-finite difference scheme with third-order Runge–Kutta time-stepping (Shi et al. 2012) to perform the simulation by solving the linear shallow water equations. In the numerical computation, the time step was fixed to one second. We used one arc-minute grid bathymetry data resampled from the 15 arc-second gridded GEBCO 2021 data (GEBCO Compilation Group 2021).

### Modeling the Lamb wave

We analyzed the relation between the peak amplitudes and the locations of the barometers. Figure 1a shows that the amplitudes were, roughly, inversely proportional to the square root of the distance from Tonga. However, the amplitudes observed at some barometers differ from the regression. This implies that local environments, such as atmospheric conditions or topography, could influence the Lamb wave amplitude.

We assumed a plan air pressure wave $P_{\mathrm{air}}$ travels along the radial direction $\phi_i$ at a translation speed $v=310$ m/s from the volcano to location $i=\left(x_i,y_i\right)$, where the origin is the volcano, and the $x$ and $y$-axes are taken as east and north, respectively. The angle $\phi_i$ is measured from the north. The $\phi_i$ is obtained by the spherical law of cosines, which is given by

$$\cos\phi_i=\frac{\cos\delta-\cos\alpha\cdot\cos\beta}{\sin\alpha\cdot\sin\beta}, \tag{4}$$

where $\delta$ and $\alpha$ are the distances from the volcano $\left(x_v,y_v\right)$ in longitude and latitude directions, and $\beta$ is the distance between $i$ and $\left(x_v,y_v\right)$. For S-net stations, $\phi_i$ is approximate 45°, so we set $\phi_i=$ N45° W in our simulation. The air pressure wave $P_{\mathrm{air}}$ from the volcano to location $i$ was given by

$$P_{\mathrm{air}}(r,t)=h_i^{\mathrm{A}}e^{-\frac{(r-vt)^2}{2\sigma^2}}+h_i^{\mathrm{B}}e^{-\frac{(r-vt+3\sigma)^2}{2\sigma^2}}+h_i^{\mathrm{C}}e^{-\frac{(r-vt-3\sigma)^2}{2\sigma^2}}, \tag{5}$$

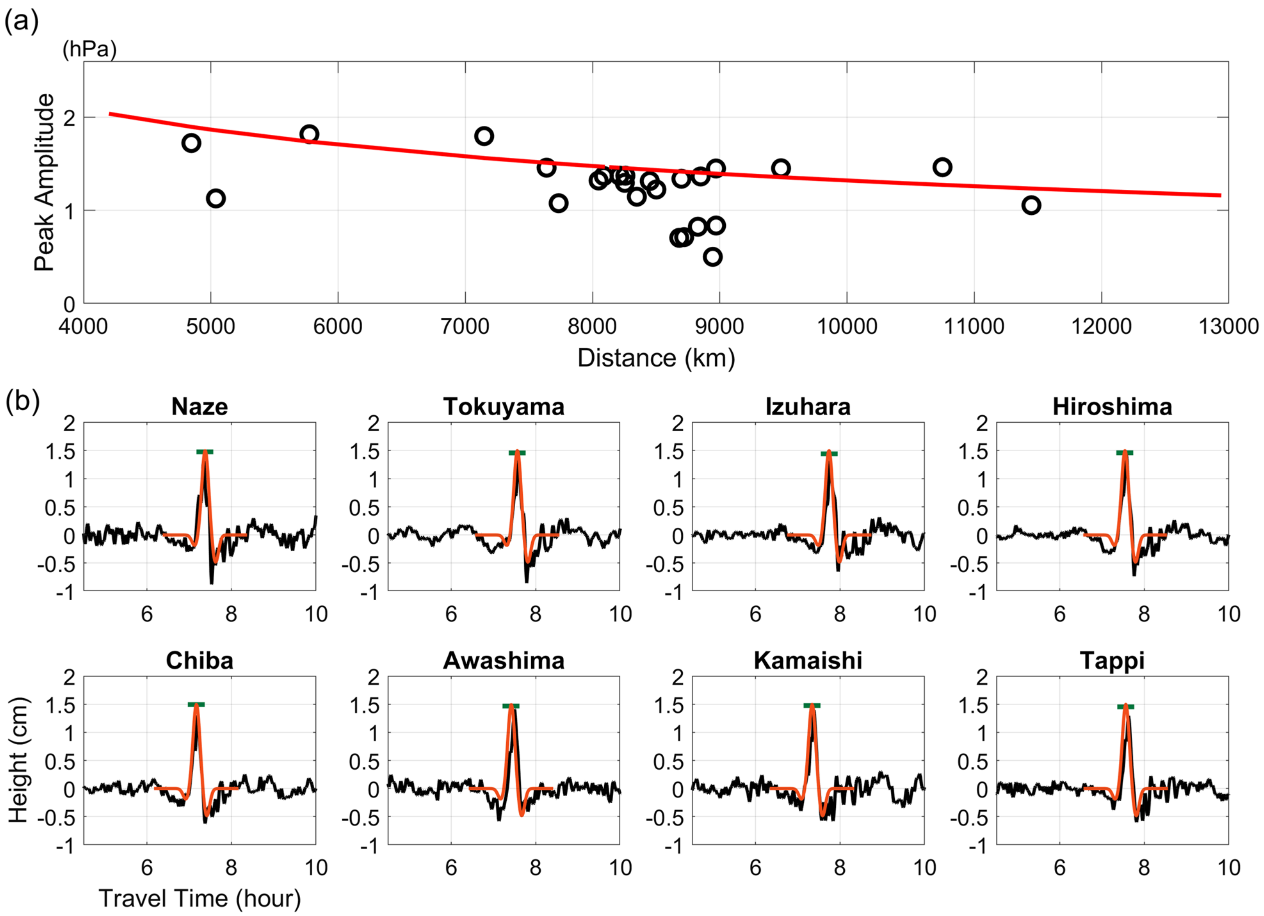

**Fig. 1** **a** The black circles represent the peak amplitude of the observed air pressures relative to the distances between the barometers and the Tongan volcano. The red line is the regression line of the peak amplitude developed by applying the attenuation relationship $h_A = h_0 R^{-0.5}$, where $h_0$ is assumed to be 132 hPa, and $R$ is the distance from the source. **b** The black and red lines display the observed and simulated air pressures in Japan. The green bars indicate the peak amplitude estimated by the regression. The station locations are shown in Additional file 1: Fig. S1

where $r$ is the distance from the volcano along $\phi_i$, $\sigma$ was set to 90 km, and $h_i^A$, $h_i^B$, and $h_i^C$ were determined based on the observed waveforms at locations $i$. We assumed the amplitude to be constant in the vicinity of Japan and set $h_i^A$, $h_i^B$, and $h_i^C$ to 1.5, $-0.2$, and $-0.5$ hPa, respectively, to reproduce the observed Lamb wave well.

## Synthetic tests

### The amplitude change of the pressure-forced waves

The pressure-forced wave is the sea surface disturbance induced by a moving air pressure wave, such as the Lamb wave (Proudman 1929). It has been found that the amplitude of the pressure-forced wave is influenced by the ratio of the air pressure speed and the long wave speed (Vilibić 2008; Vennell 2010), i.e., $\mathrm{Fr} = U\Big/\sqrt{gh}$, where $U$ and $\sqrt{gh}$ are the speeds of the air pressure wave and the long wave, respectively. Proudman resonance occurs when $\mathrm{Fr} = 1$ (Proudman 1929). Otherwise, when $\mathrm{Fr} \neq 1$, the amplitude of the pressure-forced wave is larger when Fr is closer to 1 (Vilibić 2008; Vennell 2010). Since the Lamb wave traveled at an almost constant speed of approximately 310 m/s (Matoza et al. 2022; Lynett et al. 2022; Kubota et al. 2022), Fr was controlled by the water depth. Assuming $U = 310$ m/s, the amplitude is larger when $\sqrt{gh}$ is closer to 310 m/s. This means that the amplitude of the pressure-forced wave will be more strongly amplified when the water depth is closer to 9.8 km.

### The effect of depth change: from deep to shallow water

When the water depth changes, the pressure-forced wave adjusts its amplitude to fit the new depth. We performed a synthetic test of a plane air pressure wave traveling on a domain of approximately 1112 by 6646 km in $y$ and $x$ directions, respectively. The bathymetry resolution is one arc-minute. We set a 5° west–east direction, updip slope from a depth of 4 km to 1 km at $x = 3002$ km in the

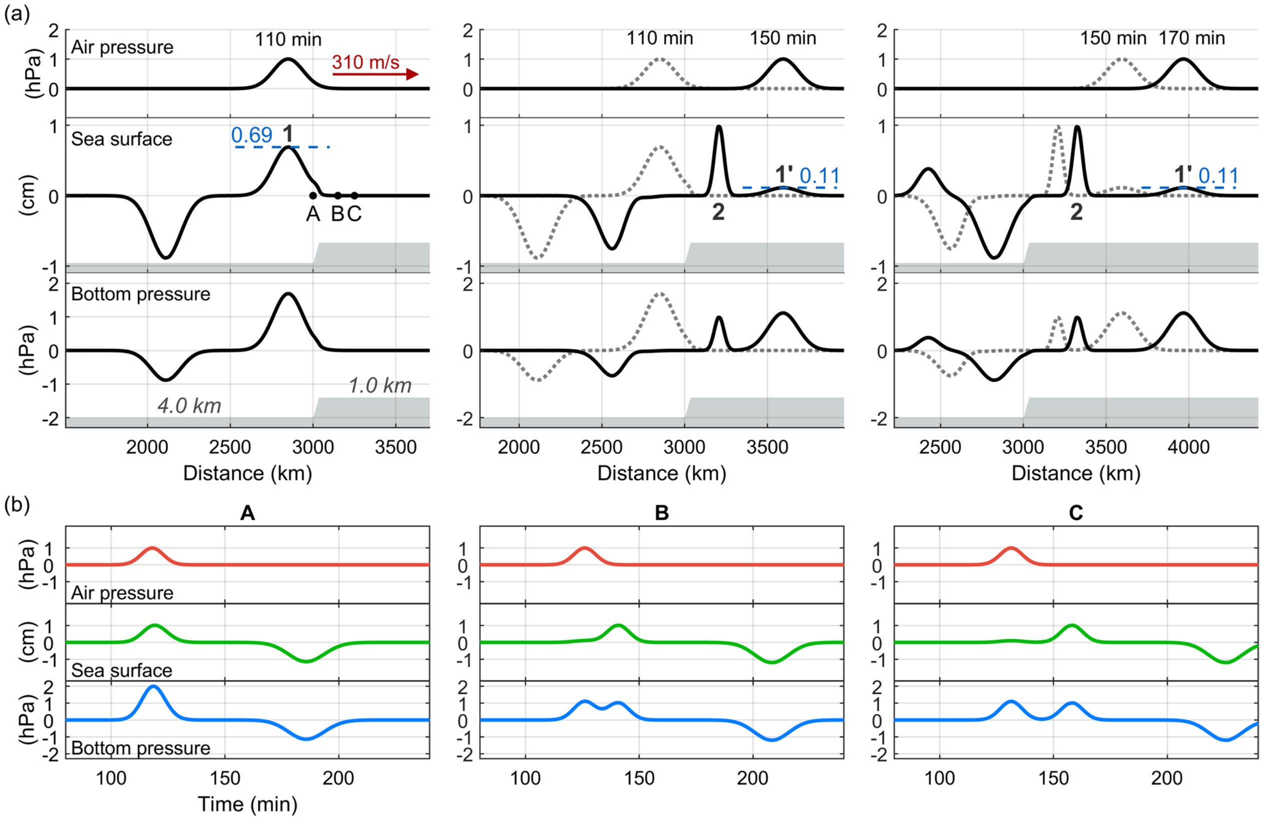

**Fig. 2** The synthetic test of an air pressure wave traveling at 310 m/s passing over a 5° updip slope from a depth of 4 km to a depth of 1 km. **a** The wave profiles of air pressure (upper row), sea surface (middle row), and bottom pressure (lower row) along *x*-direction extracted at $y = 556$ km. The times on the top of the air pressure wave indicate the origin time of the snapshots of the solid or dotted lines. The waves marked with 1, $1'$, and 2 are the incident pressure-forced wave, transmitted pressure-forced wave, and the generated ocean gravity wave, respectively. A, B, and C in the left column indicate the locations where we measured the time-series waveforms shown in **b**. **b** The waveforms at locations A (left), B (middle), and C (right). The red, green, and blue lines represent the waveforms of the air pressure wave, sea surface height, and bottom pressure, respectively

domain. The air pressure wave is a Gaussian-shaped wave given by Eq. (5) with $\sigma = 90$ km, $h_i^{A} = 1$ hPa, $h_i^{B} = 0$, and $h_i^{C} = 0$. The initial location is given by $\phi_i = \mathrm{N}90^\circ$ E ($x$-direction), $r = 820$ km when $t = 0$. We extracted the wave profile at the center of the y direction, where $y = 556$ km. Figure 2 shows the synthetic test of an air pressure wave traveling at 310 m/s passing over the slope. Figure 2a illustrates the different snapshots of wave profiles. The moving air pressure wave induced the incident pressure-forced wave (wave 1), which travels at the same speed as the air pressure wave. When wave 1 passed the slope, it split into waves $1'$ and 2. Wave $1'$ was the transmitted pressure-forced wave traveling at the same speed at shallow depths. Wave 2 was the ocean gravity wave generated when wave 1 passed the slope. Because wave 2 traveled at the long wave speed, slower than wave $1'$, it was separated from and propagated behind wave $1'$.

The amplitude of the pressure-forced wave decreased from 0.69 to 0.11 cm when the water depth changed from 4 to 1 km. The sea surface height of wave 2 was much larger than that of wave $1'$. However, the bottom pressure is a result of the water pressure over the water column and the air pressure. Because wave $1'$ traveled with the air pressure wave at the same speed, the pressures from wave $1'$ and the air pressure wave were superposed into a larger wave as recorded by the bottom pressure, as shown in the lower row of Fig. 2a. The snapshots at 150 min and 170 min show that the wave amplitude of the bottom pressure associated with wave $1'$ was comparable to the bottom pressure from wave 2.

We computed the time-series waveforms of the air pressure, sea surface height, and bottom pressure at locations A, B, and C, as shown in Fig. 2a (left). Location A is at the lower edge of the slope, and locations B and C are at shallower depths 150 and 250 km away from A, respectively. Figure 2b shows that the waveforms change with distance after passing the slope. Location A exhibits only the incident pressure-forced wave (wave 1). This shows that the wave did not split until it passed the slope. Location B displays a split waveform consisting of waves 1′ and 2. The two waves overlapped because of the short distance from the slope. At location C, the two waves were separated. The difference in the arrival times between wave 1′ and wave 2 increases with the distance from the slope. In water 1 km deep, the two waves took approximately 250 km to separate.

The test supports the findings reported by Yamada et al. (2022) that the tsunami signals were delayed at the tide gauges. Note that the tide gauges record only changes at the sea surface. Because the pressure-forced wave was very small and easy to overlook in the sea surface height, the ocean gravity waves generated in shallow water were regarded as the leading tsunami signals at the tide gauges. On the other hand, in the OBP data, the pressure-forced waves were regarded as the leading tsunami waves since the air–sea coupling was stronger at deep water and the pressure-forced waves were as large as the ocean gravity waves. As a result, the two separated waves were observed by OBP stations. Additional file 1: Fig. S4 shows the wave distribution at snapshot 110 min. Except for the reflection on the left boundary, no noticeable effects appear on the lateral (up and bottom) boundaries. The results are independent of the width of the simulation domain.

## The effect of depth change: from shallow to deep water

When the air pressure wave is excited by subaerial volcanoes or travels from land to ocean, it travels from shallow to deep water. We set a 5° west–east direction, downdip slope from a depth of 1 km to 4 km slope at $x = 3002$ km in the domain identical to that used in "The effect of depth change: from deep to shallow water" section. In addition, the assumed air pressure wave is also the same as that used in "The effect of depth change: from deep to shallow water" section. In Fig. 3, we performed a synthetic test in which an air pressure wave travels at 310 m/s passing the slope. Figure 3a illustrates different snapshots of the wave profiles. An incident pressure-forced wave (wave 1) was induced by the moving air

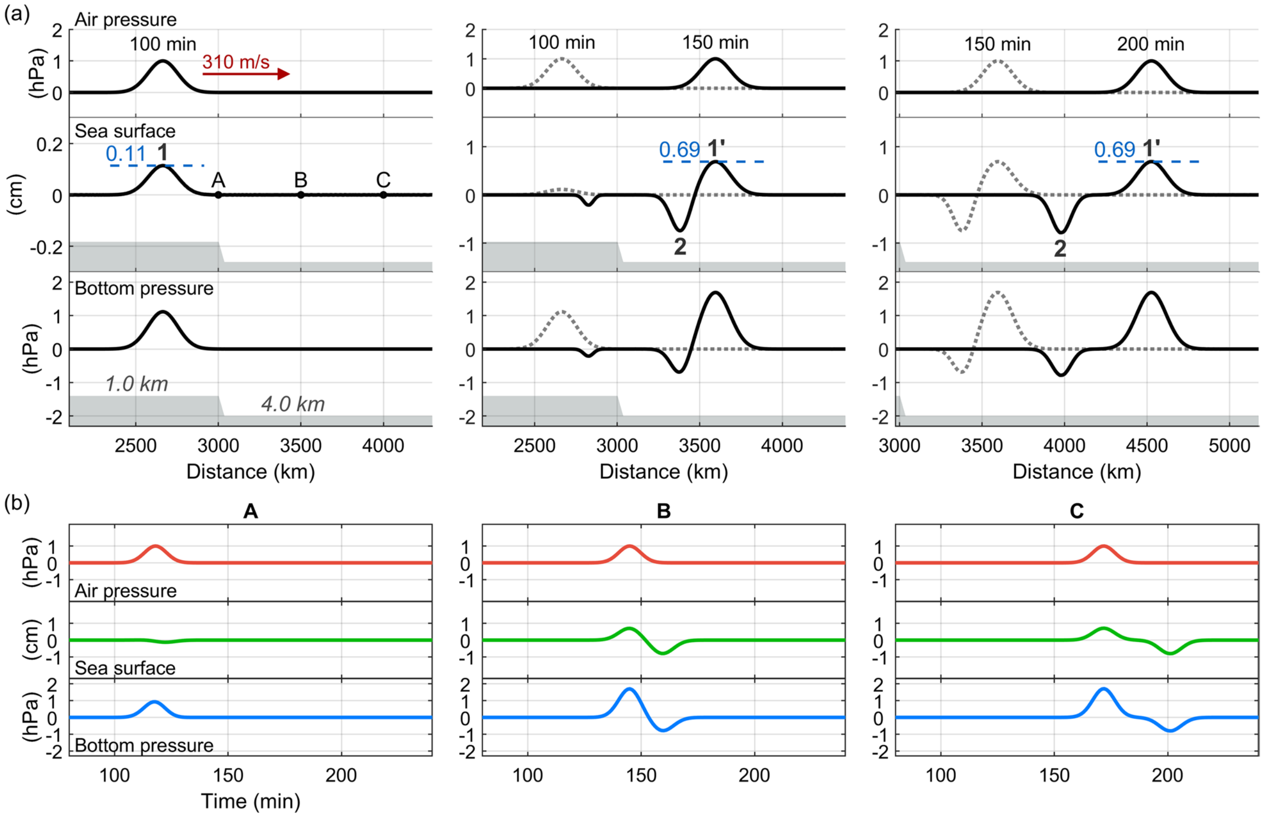

**Fig. 3** The synthetic test of an air pressure wave traveling at 310 m/s passing a 5° downdip slope from 1 to 4 km depth. **a** The wave profiles of air pressure (upper row), sea surface (middle row), and bottom pressure (lower row) along *x*-direction extracted at $y = 556$ km. The times on the top of the air pressure wave indicate the origin time of the snapshots of the solid or dotted lines. The waves marked with 1, 1′, and 2 are the incident pressure-forced wave, transmitted pressure-forced wave, and the generated ocean gravity wave, respectively. A, B, and C in the left column indicate the locations where we measured the time-series waveforms shown in **b**. **b** The waveforms at locations A (left), B (middle), and C (right). The red, green, and blue lines represent the waveforms of the air pressure wave, sea surface height, and bottom pressure, respectively

pressure wave and traveled at the same speed as the air pressure wave. Wave 1 splits into a transmitted pressure-forced wave (wave 1′) and an ocean gravity wave (wave 2) when passing the slope. The amplitude of the pressure-forced wave increased from 0.11 cm (wave 1) to 0.69 cm (wave 1′). The increased water volume was conserved by generating a polarity-reversed ocean gravity wave (wave 2). Since wave 2 traveled at the long wave speed, which was slower than wave 1′, it separated from wave 1′ at the 200 min mark.

Figure 3b shows the air pressure, sea surface, and bottom pressure waveforms at locations A, B, and C marked in the left column in Fig. 3a. Location A is at the upper edge of the slope, and locations B and C are at deeper depths 500 and 1000 km east of A, respectively. Location A recorded only the pressure-forced wave (wave 1). It shows that wave 1 did not split until passing the slope. At location B, the pressure-forced wave was amplified, and a negative ocean gravity wave (wave 2) was recorded. The waveforms at location C show that the two waves were separated. After reaching a water depth of 4 km, the two waves separated at approximately a distance of 800 km from the slope. On the other hand, the two waves separated after only approximately 250 km for a water depth of 1 km (see "The effect of depth change: from deep to shallow water" section) because of the larger speed difference between the air pressure wave and the long wave.

In Figs. 2 and 3, the sea surface heights of the pressure-forced wave were 0.11 cm at 1 km depth and 0.69 cm at 4 km depth. This suggests that when the pressure-forced wave encounters a change in water depth, its amplitude is adjusted to fit the new depth. Simultaneously, an ocean gravity wave is generated to conserve the water volume change accompanied by the amplitude change.

## Case study: the Tsunami near Japan after the Tonga eruption

After the eruption in Tonga, the S-net OBPGs observed tsunami waves in different shapes. To understand the mechanism of the deformation of the waves, we performed a case study of the tsunami induced by the air pressure wave near the Japan Trench using actual bathymetry. We simulated the domain ranged between 127°–155° E and 23°–47° N as shown in Additional file 1: Fig. S1, where the boundaries were at least 900 km from the stations. We applied Eq. (5) to reconstruct the local air pressure wave in the vicinity of Japan and used the initial source assumption as addressed in "Modeling the Lamb wave" section. The moving air pressure wave induced a pressure-forced wave on the ocean, which generated an ocean gravity wave when passing the Japan Trench.

The speed of an ocean gravity wave rapidly decreases when it encounters a steep slope, such as a trench. To quantify the wave separation, we estimated the travel time difference between the ocean gravity wave and the pressure-forced wave for the area between the coast of the Tohoku region and the Japan Trench. We simplified the depth effects by assuming that the separation between the ocean gravity wave and the pressure-forced wave begins after the incident pressure-forced wave passing $r_\zeta$, the deepest location of the trench along $r$. We considered the Lamb wave speed $U$ to be constant, and the travel time difference ($\Delta t$) between the ocean gravity wave and the pressure-forced wave for the travel distance from $r_\zeta$ to a location of interest on $r$, i.e., $r_i$, is given by:

$$\Delta t(r) = \int_{r_\zeta}^{r_i} \Delta s dr, \tag{6}$$

$$\Delta s = \frac{1}{\sqrt{gh(r)}} - \frac{1}{U}. \tag{7}$$

The travel time difference per unit distance ($\Delta s$) grows rapidly from deep to shallow water, as shown in Additional file 1: Fig. S2. $\Delta s$ becomes significantly large when the depth is shallower than 0.1 km. However, in most cases, the travel time difference is generally proportional to the travel distance.

Figure 4a shows the locations of the S-net stations. We illustrated the stations and regions with different colors for different $\Delta t$ values. Figure 4b–e illustrates the waveforms of the stations shown in Fig. 4a connected by dark lines from north to south. Figure 4b–e shows different stages of wave splitting in observed and simulated OBP waveforms (blue lines). At the stations colored in white, the travel time difference is smaller than 6 min, and there is no wave splitting in the observed and simulated waveforms. The travel time difference is slightly larger (6–12 min) at the green stations, which show wave deformation due to the overlap of separated waves in both observed and simulated OBP waveforms. The wave splitting becomes evident at the yellow and orange stations due to the significant travel time difference in these regions. The two waves are separated at the red stations, showing two clear waves in the observation and simulation.

Figure 5 illustrates snapshots of the observed and simulated waveforms at station S2N01, which is marked with a cyan circle in Fig. 4a. The pressure-forced wave was recorded with the air pressure wave as the small leading wave in the OBP data. The ocean gravity wave passed S2N01 after the pressure-forced wave. As a result, a smaller pressure-forced wave (420–445 min) and a separated ocean gravity wave (445–475 min) were recorded.

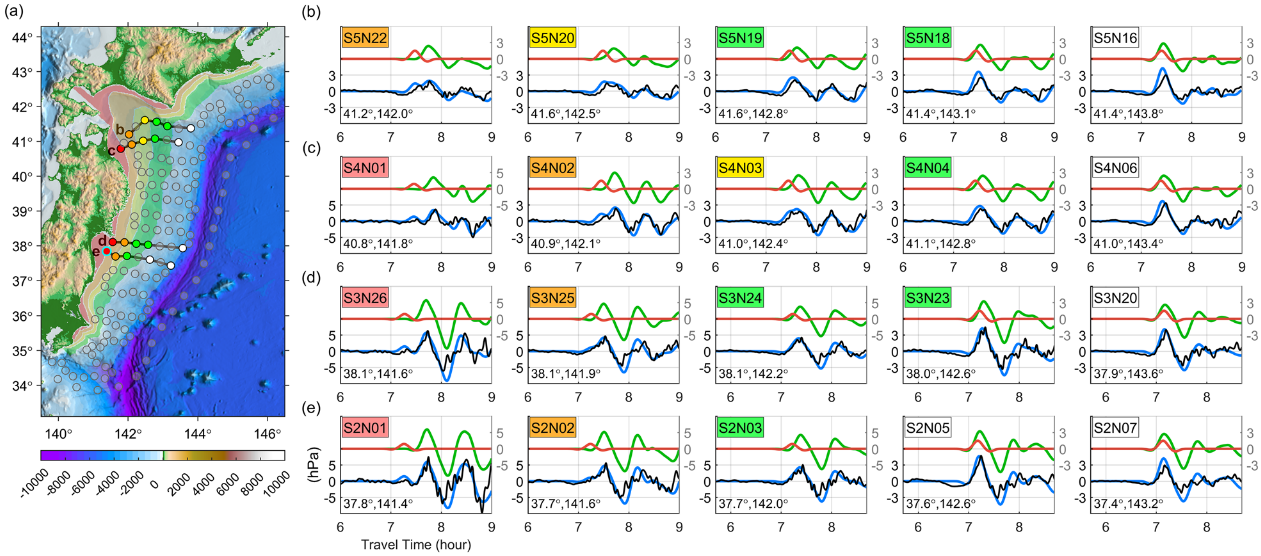

**Fig. 4** S-net stations and observed OBP waveforms compared to the simulated waveforms of air pressure, sea surface, and bottom pressure. **a** The circles represent the locations of S-net stations. The areas shaded by white, green, yellow, orange, and red indicate the areas where $\Delta t$ was < 6, 6–12, 12–18, 18–30, and > 30 min, respectively. The stations connected with dark lines are those color coded to match the corresponding $\Delta t$ values. The waveforms of those stations are shown in **b**–**e** from north to south. The light blue circle indicates the location of S2N01. **b**–**e** The waveforms of the stations that are connected with dark lines from north to south in **a**. Black lines illustrate the observed bottom pressure data. Red, green, and blue lines are the input air pressure wave, simulated sea surface heights, and simulated bottom pressures, respectively. The right y-axes indicate the scale of the red and green lines. The background colors of the station names correspond to the circles' fill colors in **a**

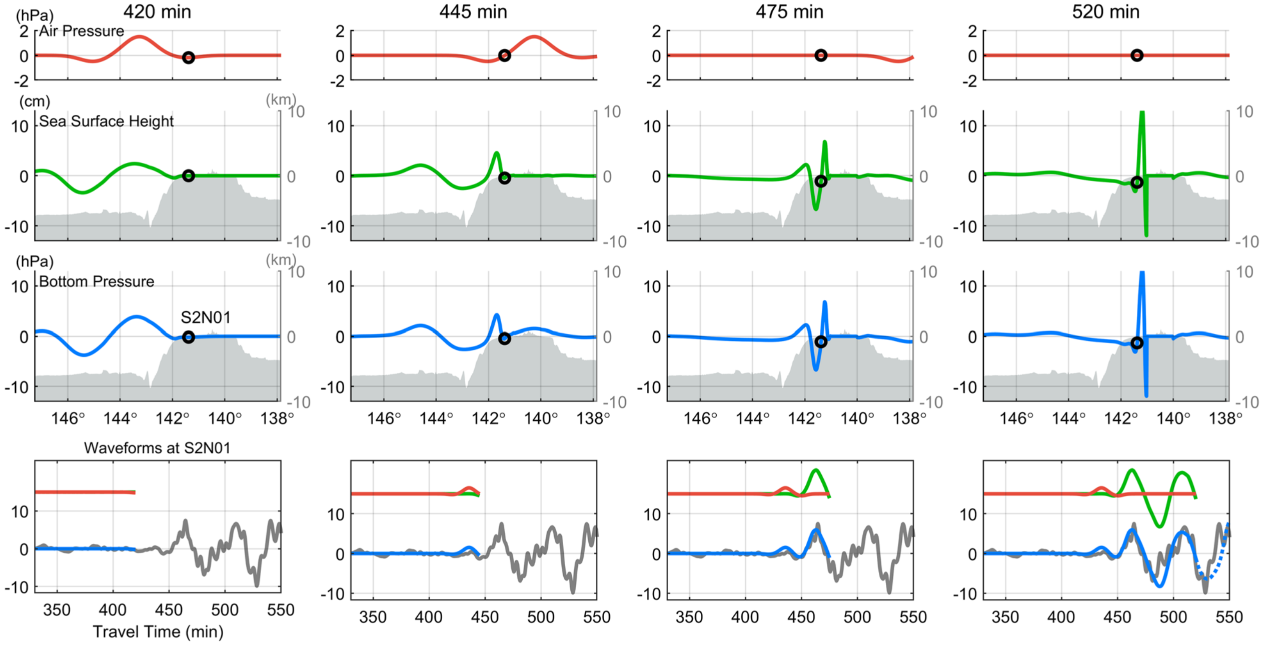

**Fig. 5** The top three rows exhibit the simulated wave profiles of the air pressure wave, sea surface height, and bottom pressure in different snapshots. The gray shaded areas indicate the bathymetry profiles with height marked by the *y*-axis on the right. The bottom row displays the waveforms at S2N01. Dark lines in the bottom plots represent the observed waveform, and the red, green, and blue lines indicate the air pressure, sea surface height, and bottom pressure, respectively

Our simulation reproduced these two waves and could extract the sea surface height from ocean bottom pressure data.

Wave deformation due to wave splitting was also observed by the DONET. However, because the DONET stations were close to the Nankai Trough (< 150 km), the travel time differences were small; thus, we could only find slight wave deformation at some stations located farther from the trough, as shown in Additional file 1: Fig. S3.

## Conclusions

The eruption of the Hunga Tonga-Hunga Ha'apai volcano caused an unusually fast tsunami throughout the Pacific. The observation from the OBPGs near the Japan Trench recorded the deformation of tsunami waves. We performed synthetic tests to investigate the tsunami wave deformation mechanism. The synthetic tests explained the wave deformation and splitting observed by S-net. We reproduced the observations of OBPGs near the Japan Trench following the 2022 Tonga eruption using a simplified air pressure model and actual bathymetry.

Our synthetic tests explained the wave splitting mechanism: the changes in water depth generate the ocean gravity wave and lead to wave split. We summarize the process when the pressure-forced wave crosses over changes in water depth:

1. The amplitude of the pressure-forced wave is adjusted to the new water depth.
2. The amplitude change is accompanied by the generation of an ocean gravity wave because of the conservation of water volume.
3. The ocean gravity wave travels slower and becomes separated from the pressure-forced wave.

This was the first time that OBPGs widely observed Lamb wave-induced tsunamis. In addition, the S-net observed the waveforms of different splitting processes after the pressure-forced wave passed the Japan Trench. The abundant observations by S-net provided excellent information for a better understanding of the splitting mechanism. We utilized the observations to validate our simulations, and our simulations sufficiently reproduced the observed waveforms for different splitting processes. To prevent from the influences from the boundaries of the simulation domain, the stations are sufficiently far from the boundaries (> 900 km for case study in Japan). In addition, we focus on the leading part of the waveforms. As a result, the influences from boundaries were minimized, and the results are independent of the simulation domain.

The synthetic tests suggest that air pressure waves originating from land or across the continents can also induce tsunamis. When a pressure-forced wave propagates from shallow to deep water, its amplitude grows, generating an ocean gravity wave with polarity-reverse. This implies that the induced tsunami wave amplitude is limited when the air pressure wave only travels over shallow water. Future works on tsunamis in the Atlantic Ocean region, such as those occurring in the Caribbean and the Mediterranean Sea, can help us understand tsunamis induced by the air pressure waves traveling from land.

### Abbreviations

| | |
|---|---|
| USGS | U.S. Geological Survey |
| OBP | Ocean bottom pressure |
| OBPGs | Ocean bottom pressure gauges |
| IRIS | Incorporated Research Institutions for Seismology |
| JCG | Japan Coast Guard |
| S-net | Seafloor Observation Network for Earthquakes and Tsunamis along the Japan Trench |
| DONET | Dense Oceanfloor Network for Earthquakes and Tsunamis |
| GEBCO | General Bathymetric Chart of the Oceans |

## Supplementary Information

The online version contains supplementary material available at https://doi.org/10.1186/s40623-023-01775-x.

**Additional file 1: Figure S1.** The circles indicate the station locations in Fig. 1. The fill color of each circle represents the estimated air pressure wave speed estimated by considering the great circle distance between the station and the volcano. The dotted rectangle indicates the simulation in the case study of Japan after the Tonga eruption. **Figure S2.** The change of travel time difference per unit distance $\Delta s$ (min/km) relative to water depth h. **Figure S3.** DONET stations and observed OBP waveforms compared to the simulated waveforms of air pressure, sea surface, and bottom pressure. (a) The circles represent the locations of DONET stations. The areas shaded by white, green, and yellow indicate the zones of $\Delta t(s)$ of < 6, 6–12, and > 12 min, respectively. The stations connected with dark lines are the circles filled with the color corresponding to their $\Delta t$. The waveforms of those stations are shown in Fig. S3b, c from west to east. (b, c) The waveforms of the stations connected with dark lines from west to east in Fig. S3a. Black lines illustrate the observed bottom pressure data. Red, green, and blue lines are the input air pressure wave, simulated sea surface heights, and simulated bottom pressures. The background color of the station name corresponds to the circle's fill color in Fig. S3a. **Figure S4.** The wave height distribution at the snapshot at 110 min in the synthetic test of the air pressure wave travels from deep to shallow water as shown in Fig. 2. The air pressure wave travels from left to right. The contour lines at around $x = 3002$ km indicate the 5° updip slope, where the water depth changes from 4 km on the left to 1 km on the right. The green line indicates the profile interval in Fig. 2a (left plot). The waves from right to left are the positive pressure-forced wave (Wave 1 in Fig. 2), the negative ocean gravity wave, and the positive pressure-forced wave reflected on the left boundary.

**Acknowledgements**

We would like to thank the National Research Institute for Earth Science and Disaster Resilience, Japan Meteorological Agency, Weathernews Inc., Japan Coast Guard, IRIS, and National Oceanic and Atmospheric Administration for providing their data. We appreciate the valuable comments and suggestions from the editor Dr. Tatsuhiko Saito, reviewer Dr. Matías Carvajal, and an anonymous reviewer. T.-C. Ho appreciates the visualization suggestions from Dr. Yi-Kai Hsieh.

### Author contributions
Conceptualization: TH, MY. Data curation: TH, MY. Formal analysis: TH. Methodology: TH. Resources: NM, MY. Supervision: NM. Visualization: TH. Writing—original draft: TH. Writing—review and editing: MY, NM. All authors read and approved the final manuscript.

### Funding
This study was supported by JSPS KAKENHI Grant No. 21K21353. This work was partly funded by DPRI-ERI cooperative research 2021-K-01.

### Availability of data and materials
The air pressure data used in the present study are from IRIS (https://ds.iris.edu/ds/nodes/dmc/; http://ds.iris.edu/gmap/) and networks of AK, CU, G, II, IU, SB, UO, US, and the Japan Coast Guard (https://near-goos1.jodc.go.jp/index.html) and network of tide data. The OBP data are from S-net (https://doi.org/10.17598/NIED.0007) and DONET (https://doi.org/10.17598/NIED.0008), maintained by the National Research Institute for Earth Science and Disaster Resilience (NIED). The bathymetry is resampled from the gridded data of GEBCO 2021 (global bathymetric product released by the General Bathymetric Chart of the Oceans) (GEBCO Compilation Group 2021). The numerical model used in this research can be accessed and downloaded through the website FUNWAVE-TVD (https://fengyanshi.github.io/build/html/index.html).

## Declarations

### Ethics approval and consent to participate
Not applicable.

### Consent for publication
Not applicable.

### Competing interests
The authors declare that they have no competing interests.

### Author details
[1]Disaster Prevention Research Institute, Kyoto University, Kyoto, Japan.

Received: 22 December 2022 Accepted: 19 January 2023

### References
Carvajal M, Sepúlveda I, Gubler A, Garreaud R (2022) Worldwide signature of the 2022 Tonga volcanic tsunami. Geophys Res Lett 49(6):e2022GL098153. https://doi.org/10.1029/2022GL098153
Garrett CJR (1970) A theory of the Krakatoa tide gauge disturbances. Tellus 22(1):43–52. https://doi.org/10.1111/j.2153-3490.1970.tb01935.x
GEBCO Compilation Group (2021) GEBCO 2021 grid. https://doi.org/10.5285/c6612cbe-50b3-0cff-e053-6c86abc09f8f
Gill AE (1982) Atmosphere-ocean dynamics, vol 30. Academic press, Amsterdam
Hibiya T, Kajiura K (1982) Origin of the Abiki phenomenon (a kind of seiche) in Nagasaki Bay. J Oceanogr Soc Jpn 38(3):172–182. https://doi.org/10.1007/BF02110288
Kubota T, Saito T, Nishida K (2022) Global fast-traveling tsunamis driven by atmospheric Lamb waves on the 2022 Tonga eruption. Science 377(6601):91–94. https://doi.org/10.1126/science.abo4364
Lamb H (1911) On atmospheric oscillations. Proc R Soc Lond Ser A Contain Pap Math Phys Character 84(574):551–572. https://doi.org/10.1098/rspa.1911.0008
Lynett P, McCann M, Zhou Z, Renteria W, Borrero J, Greer D, Fa'anunu O, Bosserelle C, Jaffe B, La Selle S, Ritchie A, Snyder A, Nasr B, Bott J, Graehl N, Synolakis C, Ebrahimi B, Cinar EG (2022) Diverse tsunamigenesis triggered by the Hunga Tonga-Hunga Ha'apai eruption. Nature 609(7928):728–733. https://doi.org/10.1038/s41586-022-05170-6
Matoza RS, Fee D, Assink JD, Iezzi AM, Green DN, Kim K, Toney L, Lecocq T, Krishnamoorthy S, Lalande J-M, Nishida K, Gee KL, Haney MM, Ortiz HD, Brissaud Q, Martire L, Rolland L, Vergados P, Nippress A, Park J, Shani-Kadmiel S, Witsil A, Arrowsmith S, Caudron C, Watada S, Perttu AB, Taisne B, Mialle P, Le Pichon A, Vergoz J, Hupe P, Blom PS, Waxler R, De Angelis S, Snively JB, Ringler AT, Anthony RE, Jolly AD, Kilgour G, Averbuch G, Ripepe M, Ichihara M, Arciniega-Ceballos A, Astafyeva E, Ceranna L, Cevuard S, Che I-Y, De Negri R, Ebeling CW, Evers LG, Franco-Marin LE, Gabrielson TB, Hafner K, Harrison RG, Komjathy A, Lacanna G, Lyons J, Macpherson KA, Marchetti E, McKee KF, Mellors RJ, Mendo-Pérez G, Mikesell TD, Munaibari E, Oyola-Merced M, Park I, Pilger C, Ramos C, Ruiz MC, Sabatini R, Schwaiger HF, Tailpied D, Talmadge C, Vidot J, Webster J, Wilson DC (2022) Atmospheric waves and global seismoacoustic observations of the January 2022 Hunga eruption, Tonga. Science 377(6601):95–100. https://doi.org/10.1126/science.abo7063
Monserrat S, Vilibić I, Rabinovich AB (2006) Meteotsunamis: atmospherically induced destructive ocean waves in the tsunami frequency band. Nat Hazards Earth Syst Sci 6(6):1035–1051. https://doi.org/10.5194/nhess-6-1035-2006
Proudman J (1929) The effects on the sea of changes in atmospheric pressure. Geophys Suppl Mon Not R Astron Soc 2(4):197–209
Rabinovich AB (2020) Twenty-seven years of progress in the science of meteorological tsunamis following the 1992 Daytona Beach event. Pure Appl Geophys 177(3):1193–1230. https://doi.org/10.1007/s00024-019-02349-3
Saito T, Kubota T, Chikasada NY, Tanaka Y, Sandanbata O (2021) Meteorological tsunami generation due to sea-surface pressure change: three-dimensional theory and synthetics of ocean-bottom pressure change. J Geophys Res Oceans 126(5):e2020JC017011. https://doi.org/10.1029/2020JC017011
Shi F, Kirby JT, Harris JC, Geiman JD, Grilli ST (2012) A high-order adaptive time-stepping TVD solver for Boussinesq modeling of breaking waves and coastal inundation. Ocean Model 43:36–51. https://doi.org/10.1016/j.ocemod.2011.12.004
Tanioka Y, Yamanaka Y, Nakagaki T (2022) Characteristics of the deep sea tsunami excited offshore Japan due to the air wave from the 2022 Tonga eruption. Earth Planets Space 74(1):1–7. https://doi.org/10.1186/s40623-022-01614-5
Vennell R (2010) Resonance and trapping of topographic transient ocean waves generated by a moving atmospheric disturbance. J Fluid Mech 650:427–442
Vilibić I (2008) Numerical simulations of the Proudman resonance. Cont Shelf Res 28(4–5):574–581. https://doi.org/10.1016/j.csr.2007.11.005
Vilibić I, Šepić J, Rabinovich AB, Monserrat S (2016) Modern approaches in meteotsunami research and early warning. Front Mar Sci 3:57
Woodruff I, Kirby J, Shi F, Grilli S (2018) Estimating meteo-tsunami occurrences for the us east coast. Coast Eng Proc. https://doi.org/10.9753/icce.v36.currents.66
Yamada M, Ho T-C, Mori J, Nishikawa Y, Yamamoto MY (2022) Tsunami triggered by the Lamb wave from the 2022 Tonga volcanic eruption and transition in the offshore Japan region. Geophys Res Lett 49:e2022GL098752. https://doi.org/10.1029/2022GL098752